

Partial confinement in a quantum-link simulator

Zheng Tang¹, Fei Zhu¹, Yi-Fan Luo^{2,3}, Wei Zheng^{2,3,4,*} and Li Chen^{1†}

¹*Institute of Theoretical Physics, State Key Laboratory of Quantum Optics and Quantum Optics Devices, Shanxi University, Taiyuan 030006, China*

²*Hefei National Laboratory for Physical Sciences at the Microscale and Department of Modern Physics, University of Science and Technology of China, Hefei 230026, China*

³*CAS Center for Excellence in Quantum Information and Quantum Physics, University of Science and Technology of China, Hefei 230026, China*

⁴*Hefei National Laboratory, University of Science and Technology of China, Hefei 230088, China*

Confinement/deconfinement, captivating attributes of high-energy elementary particles, have recently garnered wide attention in quantum simulations based on cold atoms. Yet, the *partial confinement*, an intermediate state between the confinement and deconfinement, remains underexplored. The partial confinement encapsulates the phenomenon that the confining behavior of charged particles is contingent upon their relative positions. In this paper, we demonstrate that the spin-1 quantum link model provides an excellent platform for exploring partial confinement. We conduct a comprehensive investigation of the physics emerging from partial confinement in both the context of equilibrium and non-equilibrium dynamics. Potential experimental setups using cold atoms are also discussed. Our work offers a simple and feasible routine for the study of confinement-related physics in the state-of-the-art artificial quantum systems subject to gauge symmetries.

I. INTRODUCTION

Confinement is a fundamental property prominently observed in quantum chromodynamics (QCD), where the interquark potential increases with their distance [1–3]. This prevents the existence of isolated quarks due to energetic instability; instead, they prefer to bind together into hadrons, either as mesons (quark-antiquark pairs) or baryons (triplets of quarks). Although the concept originated in QCD, analogous phenomena can also manifest in strongly coupled charges in quantum electrodynamics (QED) [4, 5], i.e., the charge confinement. For instance, in (3+1)D QED, increasing the coupling strength g facilitates a transition from the deconfined Coulomb phase to the confining phase at finite temperature [6]. Particularly in (1+1)D QED, also known as the Schwinger model, the absence of a magnetic field renders the system to be always strongly coupled. Consequently, apart from certain exceptional cases, the confining phase becomes quite prevalent even at zero temperature [7, 8]. Confinement and deconfinement phenomena also appear in emergent gauge theories in the strongly-correlated quantum matter. For instance, transition between valence bond solid to spin liquid phase can be understood in a picture of confinement-deconfinement transition of spinons [9, 10]. However, large scale numerical investigation of the real time dynamics of confinement or deconfinement on classical computers is challenging.

Recently, much efforts have been made to overcome this barrier via the approach of quantum simulation, which relies on systems with discrete degrees of freedom, such as cold atoms in optical lattices [11–15] or trapped ions [16, 17]. The simulation implements the lattice gauge theory through a Hamiltonian formalism called the quantum link model (QLM) [18–22], with matter particles and gauge spins being respec-

tively placed on lattice sites and links connecting neighboring sites. The realization of QLM is considered as a powerful approach for exploring strongly coupled QED [18], as strong coupling renders perturbative field theory ineffective, and hence quantum simulation can essentially circumvent the issues encountered by classical simulations, such as the sign problem in quantum Monte Carlo [23]. In these quantum-link simulators, both confinement and deconfinement have been extensively studied, encompassing theoretical [24–31] and experimental [15, 32] contexts. Particularly for the spin-1/2 QLM, the confinement-deconfinement phase transition has been experimentally observed in non-equilibrium dynamics by tuning the topological angle [15].

In this paper, we delve into an intermediate phenomenon between confinement and deconfinement, called *partial confinement*, which has hitherto remained unexplored within the context of quantum simulation. It refers to the situation where the confining or deconfining status between charges depends on their relative positions. Our study draws inspiration from the seminal work of S. Coleman in the 1976 [5], which studied half-asymptotic particles in the continuous Schwinger model. Here, we demonstrate that the one-dimensional spin-1 QLM can serve as an excellent platform for observing partial confinement: it retains the essential physics while being simple enough to be realized within the scope of current experimental capabilities. Taking the spin-1 QLM as a background, we introduce the basic concept of partial confinement and discuss the associated emergent physics, both in equilibrium and non-equilibrium dynamics.

The rest of this paper is structured as follows: Sec. II provides a review of the spin-1 quantum link model, detailing its essential physical features. In Sec. III, we delve into the equilibrium properties of partial confinement within the spin-1 QLM. Sec. IV discusses how partial confinement manifests in non-equilibrium dynamics. In Sec. V, we explore the feasibility of experimental realizations using cold atoms trapped in optical super-lattices. A brief summary can be found in Sec. VI.

* zw8796@ustc.edu.cn

† lchen@sxu.edu.cn

II. SPIN-1 QUANTUM LINK MODEL

The spin-1 quantum link chain is characterized by the Hamiltonian [18, 24, 33]

$$H = -J \sum_{j=1}^{N-1} \left(\frac{1}{\sqrt{2}} \psi_j S_j^+ \psi_{j+1} + \text{h.c.} \right) + m \sum_{j=1}^N \psi_j^\dagger \psi_j + g \sum_{j=1}^{N-1} \left[(-1)^{j+1} S_j^z + \frac{\theta}{2\pi} \right]^2, \quad (1)$$

where ψ_j denotes the local matter fields of fermions, and $S_j^{z,\pm}$ are the spin-1 Pauli operators representing the gauge spins living on the link between two neighboring sites j and $j+1$. The number of sites N must be even, allowing for the division of fermions into positrons and electrons, yielding the *particle-antiparticle picture*: for $j \in \text{even}$, $|0\rangle$ and $|1\rangle = \psi_{j \in \text{even}}^\dagger |0\rangle$ respectively represent the unoccupied and occupied states of electrons, denoted by empty circles and red disks in Fig. 1; whereas for $j \in \text{odd}$, $|1\rangle$ represents the occupation of positrons, illustrated by blue disks.

The last two terms in H respectively represent the fermion mass with $m \geq 0$ and the electric-field energy $g \sum_j E_j^2$ with $g \geq 0$ and

$$E_j = (-1)^{j+1} S_j^z + \frac{\theta}{2\pi}. \quad (2)$$

A local E_j consists of two parts: S_j^z represents the quantized electric field capable of adopting three states $|s_j = -1\rangle$, $|0\rangle$, and $|1\rangle$. The factor $(-1)^j$ indicates that the electric field E_j depends on the gauge spins in an alternating manner: E_j is aligning with S_j^z for $j \in \text{odd}$, while they differ by a minus sign for $j \in \text{even}$. The c-number θ is called the topological angle [5, 34–36], which reflects the influence of an external static electric field. Thereby, the eigenvalues of E_j can also take three real values, i.e., $\epsilon_j = (-1)^{j+1} s_j^z + \theta/2\pi$. Restricting E_j within finite status is a key advantage of the QLM, as it facilitates experimental simulation of electric fields using a finite number of discrete degrees of freedom (such as cold atoms with internal spins). In Fig. 1, the black arrows on links represent the electric-field state ϵ_j in the case of $\theta = 0$, where each left(right)-pointing arrow denotes $\epsilon = -1/2(1/2)$. Orange arrows depict the background field of $\pm 1/2$, corresponding to the cases of $\theta = \pm\pi$, respectively. A pair of opposing arrows on the same link can mutually cancel each other out.

The first term in Eq. (1) characterizes the matter-gauge interaction. This term provides the Schwinger mechanism, i.e., a pair of electron and positron merge together accompanied by the emission of gauge photons, as well as its reverse process. Photon creation/annihilation is reflected in the change of spin states via S_j^\pm .

The spin-1 QLM exhibits a U(1) local gauge symmetry generated by the local Gauss operator

$$G_j = E_j - E_{j-1} - (-1)^j \psi_j^\dagger \psi_j = (-1)^{j+1} \left[S_j^z + S_{j-1}^z + \psi_j^\dagger \psi_j \right], \quad (3)$$

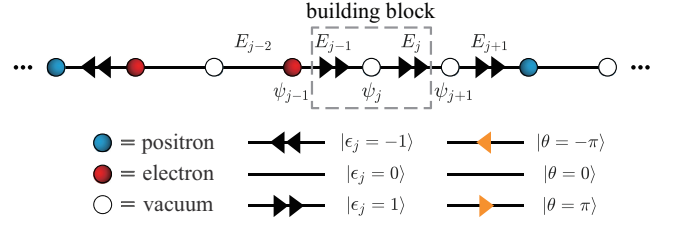


FIG. 1. Upper panel: The schematic representation of a spin-1 quantum link model in the particle-antiparticle picture. Circles denote matter fields residing on lattice sites; links between neighboring sites represent electric fields E_j realized by gauge spins S_j^z . Two adjacent gauge spins with a matter field in between constitute a building block. Lower panel: The notation convention for matter-field occupations and electric spin states.

satisfying $[G_j, H] = [G_j, G_{k \neq j}] = 0$. This ensures the invariance of the Hamiltonian under arbitrary U(1) gauge transformations $U_j = \exp(i\phi_j G_j)$. As per Eq. (3), G_j is defined within a *building block* consisting of two gauge fields $\{E_{j-1}, E_j\}$ and a matter field ψ_j in the middle [see the box with dashed lines in Fig. 1]. The quantum number of G_j , denoted by q_j , is called the static gauge charge, which is apparently a good quantum number. q_j characterizes the difference between the net electric flux $E_j - E_{j-1}$ and the matter charge $\psi_j^\dagger \psi_j$. The additional factor $(-1)^j$ arises from the opposite matter charges carried by electrons and positrons. The U(1) gauge symmetry divides the total Hilbert space into several gauge sectors, each labeled by a unique set of gauge charges $\mathbf{q} = \{q_1, q_2, \dots, q_{N-1}\}$. Notably, the sector with $\mathbf{q} = \mathbf{0}$ is called the physical sector, as now Eq. (3) aligns with the traditional Gauss's Law in the classical electrodynamics.

In some literature [24, 37–39], the QLM [Eq. (1)] is presented in an alternative form within the *particle picture*, described by the Hamiltonian

$$\tilde{H} = -J \sum_{j=1}^{N-1} \left(\frac{1}{\sqrt{2}} \psi_j^\dagger S_j^+ \psi_{j+1} + \text{h.c.} \right) + m \sum_{j=1}^N (-1)^j \psi_j^\dagger \psi_j + g \sum_j \left(S_j^z + \frac{\theta}{2\pi} \right)^2, \quad (4)$$

which relates to the particle-antiparticle Hamiltonian H [Eq. (1)] through a particle-hole transformation on odd sites, i.e. $\psi_{j \in \text{odd}} \mapsto \psi_{j \in \text{odd}}^\dagger$, as well as a transformation on even gauge spin $S_{j \in \text{even}}^+ \mapsto -S_{j \in \text{even}}^-$ and $S_{j \in \text{even}}^z \mapsto -S_{j \in \text{even}}^z$. In this framework, $\psi_j^\dagger \psi_j$ at odd sites represents the occupation below the Dirac sea, thereby exhibiting a negative energy (mass) $-m$. The creation of a hole ψ_j in the particle picture is equivalent to the creation of a positron ψ_j^\dagger in the particle-antiparticle picture. Note that both Hamiltonians, H and \tilde{H} , are mathematically equivalent for calculation purposes. Therefore, we proceed with our following analysis using the particle-antiparticle picture.

III. PARTIAL CONFINEMENT IN EQUILIBRIUM

The confining effects can be clearly demonstrated by the properties of equilibrium states in the physical sector $\mathbf{q} = \mathbf{0}$. We first focus on the simplest case of $J = 0$, where the matter and gauge fields are decoupled, thereby $\psi_j^\dagger \psi_j$ and S_j^z being conserved. We insert a pair of testing electron and positron into the vacuum, separated by a distance d , as schematically shown in Fig. 2(a). d can be positive or negative, with $d > 0$ indicating the positron is to the left of the electron, and vice versa. The case of $d = 0$ is excluded by the Pauli exclusion principle. According to Gauss's Law [Eq. (3)], the system is in the string state

$$|\psi_{\text{str}}\rangle = \begin{cases} |\cdots 0_0 1_{-1} 0_1 0 \cdots 0_1 0_{-1} 1_0 0 \cdots\rangle & \text{for } d > 0 \\ |\cdots 1_{-1} 0_1 0_{-1} 0 \cdots 0_{-1} 1_0 0_0 0 \cdots\rangle & \text{for } d < 0 \end{cases}, \quad (5)$$

where an electric string exists between the matter charges [see Fig. 2(a)]. The notation convention in a building block is $|s_{j-1}, n_j, s_j\rangle$, with s_j and n_j being the quantum numbers of S_j^z and $\psi_j^\dagger \psi_j$, respectively. For a sufficiently large m , string state is the ground state, as $m > 0$ does not favor matter-particle excitations.

The confining property is determined by the variance of the state energy $\mathcal{E} = \langle \psi | H | \psi \rangle$ on d , where the topological angle θ plays a crucial role. To be more specific, the string state has energy

$$\mathcal{E}_{\text{str}} = 2m + g|d| \left[-\text{sgn}(d) + \frac{\theta}{2\pi} \right]^2 + g(N - |d| - 1) \left[\frac{\theta}{2\pi} \right]^2, \quad (6)$$

where $\text{sgn}(x)$ is the sign function being defined as $\text{sgn}(x > 0) = 1$ and $\text{sgn}(x < 0) = -1$. When $\theta = 0$, $\mathcal{E}_{\text{str}} = 2m + g|d|$ which is linearly proportional to $|d|$, irrelevant to the sign of d , which is a typical nature of confinement. The dependence of \mathcal{E}_{str} on d is numerically confirmed by the line with circles in Fig. 3(a). Pictorially, as depicted in Fig. 2(a), confinement manifests as an increase in the length of the string with local $|\epsilon_j| = 1$, leading to an increment in the total electric energy. The string tension is defined as $\rho = \partial \mathcal{E} / \partial |d|$, which evaluates to $\rho_{\text{str}} = g$ for the string state.

The energy instability of the string state manifests in a possible decay into the meson state with lower energy. The meson configuration is

$$|\psi_{\text{meson}}\rangle = \begin{cases} |\cdots 0_0 1_{-1} 1_0 0 \cdots 0_0 1_{-1} 1_0 0 \cdots\rangle & \text{for } d > 0 \\ |\cdots 1_{-1} 1_0 0_0 0 \cdots 1_{-1} 1_0 0_0 0 \cdots\rangle & \text{for } d < 0 \end{cases}, \quad (7)$$

as illustrated in Fig. 2(a), which results from the binding of test charges to their nearest anti-particles, with the inter-particle electric string being screened. Hence, the decay process is also called the string breaking. The meson state has an energy

$$\mathcal{E}_{\text{meson}} = 4m + 2g \left[-\text{sgn}(d) + \frac{\theta}{2\pi} \right]^2 + g(N-3) \left[\frac{\theta}{2\pi} \right]^2, \quad (8)$$

which is notably independent of the distance $|d|$. For $\theta = 0$, the energy simplifies to $\mathcal{E}_{\text{meson}} = 4m + 2g$, as indicated by the

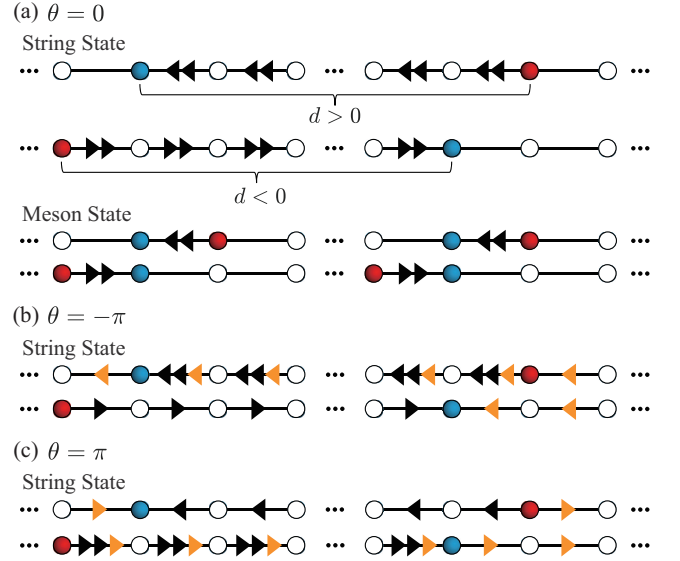


FIG. 2. The configuration of states at $J = 0$. (a) For the case of $\theta = 0$, the first and second rows depict the string states with $d > 0$ and $d < 0$, respectively. The third and fourth rows illustrate the corresponding configurations of the meson states. (b) and (c) correspond to the cases of $\theta = \mp\pi$, where only the configurations of the string states are shown.

line with triangles in Fig. 3(a). This implies a transition point

$$d_c = 2 + \frac{2m}{g(1 - \text{sgn}(d)\frac{\theta}{\pi})}. \quad (9)$$

For $|d| < |d_c|$, the string state $|\psi_{\text{str}}\rangle$ has lower energy, as it involves fewer matter particles compared to the meson state; however, for $|d| > |d_c|$, the meson state becomes more energetically favored. For $\theta = 0$, the transition point is where the two curves converge with $|d_c| = 2 + 2m/g$, as shown in Fig. 3(a).

Partial confinement occurs at $\theta = -\pi$, where the string-state energy simplifies to

$$\mathcal{E}_{\text{str}}^{\theta=-\pi} = \begin{cases} 2m + g[2d + (N-1)/4] & \text{for } d > 0 \\ 2m + g[(N-1)/4] & \text{for } d < 0 \end{cases}. \quad (10)$$

Accordingly, the string tension is $\rho_{\text{str}} = 2g$ for $d > 0$, and $\rho_{\text{str}} = 0$ otherwise. It is clearly indicated that the confining effect only occurs for $d > 0$. For $d < 0$, \mathcal{E}_{str} is independent of d , suggesting a deconfinement with $d_c = \infty$. This phenomenon, that the confining property depends on the relative positions of the opposite charges, is termed the partial confinement. Visually, as illustrated in Fig. 2(b), the string states for $d > 0$ and $d < 0$ are subjected to different electric potentials. For the former, the energy density within the string is $g(3/2)^2$, while that of the vacuum is $g(1/2)^2$, resulting in a non-vanishing string tension $\rho_{\text{str}} = 2g$, which is twice the value corresponding to the $\theta = 0$ case. For the latter, the electric fields inside and outside the string have opposite signs but with the same energy density $g(1/2)^2$, thus making \mathcal{E} being

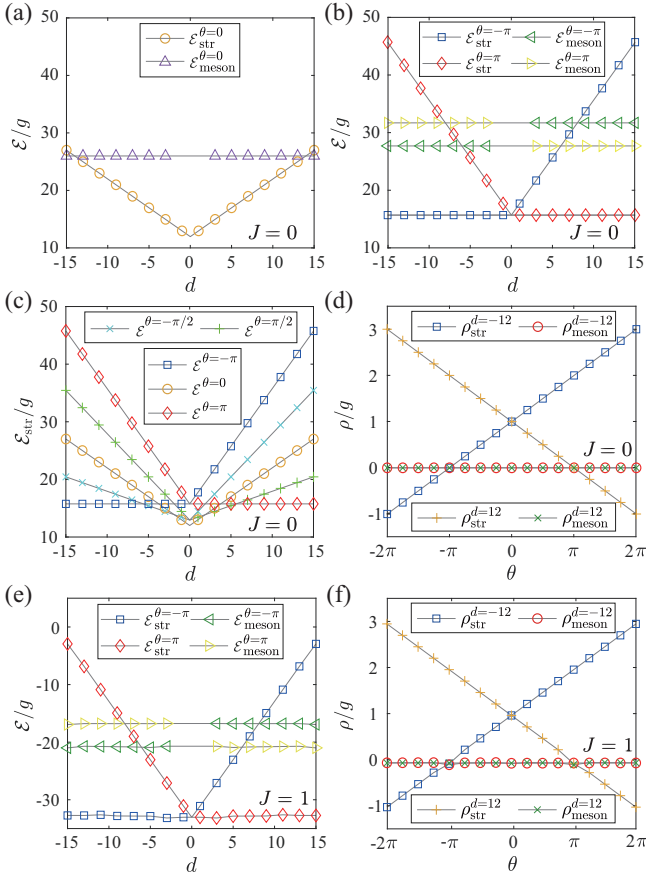


FIG. 3. Behaviors of the states' energy \mathcal{E} and string tension ρ in equilibrium with fixed $N = 16$, $g = 1$ and $m = 6g$. Panels (a)-(d) correspond to the integrable case $J = 0$: (a) displays the dependence of the string state energy \mathcal{E}_{str} and the meson state energy $\mathcal{E}_{\text{meson}}$ on d for $\theta = 0$; (b) depicts the behavior of \mathcal{E}_{str} and $\mathcal{E}_{\text{meson}}$ for $\theta = \pm\pi$; (c) shows \mathcal{E}_{str} for different values of θ ; (d) presents the string tension ρ as a function of the topological angle θ for fixed $d = \pm 12$. Panels (e)-(f) correspond to the non-integrable case $J = 1$: (e), analogous to panel (b), illustrates the string-like eigenstate energy \mathcal{E}_{str} and the meson-like eigenstate energy $\mathcal{E}_{\text{meson}}$ for $\theta = \pm\pi$; (f), analogous to panel (d), shows the string tension as a function of the topological angle θ for fixed $d = \pm 12$.

$|d|$ -invariant. In Fig. 3(b), the line with squares depicts the variation of the string state energy $\mathcal{E}_{\text{str}}^{\theta=-\pi}$ as a function of d , while the line with left-pointing triangles represents the meson state energy $\mathcal{E}_{\text{meson}}^{\theta=-\pi}$. It is evident that the string breaking can only occur in the confined regime $d > 0$, with $d_c = 2 + m/g$. The value of d_c is smaller compared to the $\theta = 0$ case, as shown in Fig. 2(b), due to the larger string tension.

Partial confinement also occurs at $\theta = \pi$, but the dependence of quantities (such as \mathcal{E} and ρ) on the sign of d is opposite to the case of $\theta = -\pi$ case, as illustrated in Fig. 2(c) and Fig. 3(b) [see lines with diamonds and squares]. The underlying mechanism can be understood in the following way. For the Hamiltonian (1), $\theta \rightarrow -\theta$ is equivalent to $S_j^+ \rightarrow S_{j+1}^+$, $S_j^z \rightarrow S_{j+1}^z$ and $\psi_j \rightarrow \psi_{j+1}$, the latter corresponds to the charge conjugation \mathcal{C} . As a result, the physics

under $\theta = -\pi$ with a given d is reproduced by $\theta = \pi$ with $-d$. This suggests that reversing θ alone can switch between confinement and deconfinement scenarios without the need to adjust the spatial ordering of charges. It would facilitate experimental observation of partial confinement since tuning the topological angle (namely tuning the external field) is generally more accessible than manipulating the particle positions in practice.

For other cases with $\theta \in (-\pi, \pi)$ and $\theta \neq |\pi|$, the string state is generally confined according to Eq. (6), with \mathcal{E}_{str} for various θ being shown in Fig. 3(c). \mathcal{E}_{str} is asymmetric about $d = 0$, with the corresponding string tension being given by $\rho_{\text{str}} = g[1 - (\theta/\pi)\text{sgn}(d)]$. The asymmetry of $\mathcal{E}(d)$ and $\rho_{\text{str}}(d)$ for $\theta \neq 0$ originates from the breaking of both \mathcal{C} and \mathcal{P} symmetry due to the topological angle θ , where \mathcal{P} is the parity operator acting as $S_j^+ \rightarrow S_{-j-1}^+$, $S_j^z \rightarrow S_{-j-1}^z$, $\psi_j \rightarrow (-1)^j \psi_{-j}$ on the Hamiltonian (1). In Fig. 3(d), we fix $d = \pm 12$ and display the dependence of ρ on θ . One can clearly observe that the partial confinement begins to occur at $\theta = \pm\pi$, where $\rho_{\text{str}} = 0$. For a larger θ , i.e., $|\theta| > \pi$, the string state becomes deconfined with a negative string tension. This is also intuitive, as a strong background electric field would polarize the charging pair and yield a large dipole moment.

The above results for $J = 0$ will not be qualitatively altered when we turn on the matter-gauge interaction J . When J is finite, the system lacks integrability, causing a resort to numerical calculations. By setting $J = g = 1$ and $m = 6g$, we numerically calculate the energy spectrum of the system. Although quantum fluctuations render s_j^z and n_j no longer good quantum numbers, we can still identify low-energy string-like and meson-like states, with the averaged local observables, such as $\langle S_j^z \rangle$ and $\langle \psi_j^\dagger \psi_j \rangle$, resembling the configurations of string and meson states shown in Fig. 3(b). Intuitively, the string remains but is thickened by quantum fluctuations. In Fig. 3(e), we present the energy variance of these two eigenstates \mathcal{E} on d for various θ ; Additionally, Fig. 3(f) shows the corresponding string tension ρ as a function of θ for a fixed $d = \pm 12$. A comparison between panels (b) and (e), as well as (d) and (f), clearly demonstrates that the main physical results, such as partial confinement and string breaking, are qualitatively preserved for a non-vanishing J .

It may be also necessary to elucidate the differences between the spin-1 QLM discussed here and the spin-1/2 QLM, with the latter, has been extensively studied both theoretically and experimentally [12–15, 24–27, 40, 41]. The Hamiltonian of the spin-1/2 QLM has the same form as Eq. (1), but with the spin operators S_j being spin-1/2 Pauli operators (up to a constant factor). In this case, even without an external electric field, the string state is no longer well-defined, as there always exist electric strings between the charges (inner string) and outside the charges (outer string). Commonly, the spin-1/2 QLM with the outer string pointing to the right (left) is considered to have an inherent topological angle $\theta = \pi$ ($\theta = -\pi$) [15, 25–27]. In contrast to the spin-1 case, the charge conjugation \mathcal{C} now would simultaneously change the order of the charges and the sign of θ , rendering the total energy \mathcal{E} irrelevant to the sign of d . In this sense, the spin-1 QLM may serve

as a better platform for the study of partial confinement, as it allows for independently changing the charge ordering and θ .

IV. PARTIAL CONFINEMENT IN DYNAMICS

After discussing equilibrium physics in depth, we now turn to non-equilibrium dynamics. Our objective is to explore whether the physics of partial confinement can be signified by the quantum dynamics out of equilibrium. To this end, we initialize the state $|\psi_0\rangle$ to be a string state with the positron and electron residing on the two edges of the chain with $d > 0$, i.e.,

$$|\psi_0\rangle = |\psi_{\text{str}}\rangle = |1_{-1}0_10\cdots0_10_{-1}1\rangle. \quad (11)$$

Notably, this state is an eigenstate of the Hamiltonian H when $J = 0$. We then allow the system to evolve under the government of H with $J = g = 1$. In our numerical simulations, $N = 16$, $m = 2g$ are fixed. We primarily focus on the three cases of $\theta = \{-\pi, 0, \pi\}$. According to the previous discussions, for such a string configuration $|\psi_0\rangle$ with the positron situated to the left of the electron, both $\theta = 0$ and $\theta = -\pi$ are confining, while $\theta = \pi$ is deconfining. Since flipping the sign of θ is equivalent to changing the sign of charge ordering d , as discussed in Sec. III, comparing the dynamics at $\pm\theta$ for a fixed string state can directly signify the partial confinement.

We begin by examining the expectation values of fermion occupations $\langle n_j \rangle = \langle \psi_j^\dagger \psi_j \rangle$ within the time frame $t \leq 30g^{-1}$, as shown in Fig. 4 with panels (a), (b), and (c) corresponding to the cases of $\theta = -\pi$, 0, and π . In the figures, the occupations of electrons and positrons are labeled by red and blue color bars, respectively. A prominent feature is that, for the first two confining cases (i.e., $\theta = -\pi$ and 0), the edge charges are 'locked' at the boundaries with almost no movement. In the bulk of the chain, $\langle n_j \rangle$ overall exhibits a periodic oscillation, which is indicative of the Schwinger mechanism, as labeled by the white boxes: electron-positron pairs are spontaneously created from the vacuum and then rapidly annihilated with each other. The confinement effect is also evidenced by the small lifetime of the emerged particles (anti-particles) and the fact that they cannot propagate to a wider range on the chain.

On the other hand, the case with $\theta = \pi$ [Fig. 4(c)] exhibits a strikingly different behavior. The two edge charges move towards each other until they meet at the center of the chain at about $t \approx 12g^{-1}$; after that, they reverse their directions and retreat to the boundaries. This exemplifies partial confinement effectively. At the outset, due to $\theta = \pi$, the electron and positron are deconfined, which permits their free movement toward the chain's center. As they exchange their positions at about $j = N/2$, the charges become confined. The confinement prevents their further propagation, compelling them to reverse direction. Additionally, it can be also notable from the figure that the particle occupation $\langle n_j \rangle$ at the boundaries is significantly decreased compared to the initial state after one round trip. Unlike the Schwinger oscillations in the former two cases, the back-and-forth motion of particles can now only sustain for a few cycles and lacks robust periodicity.

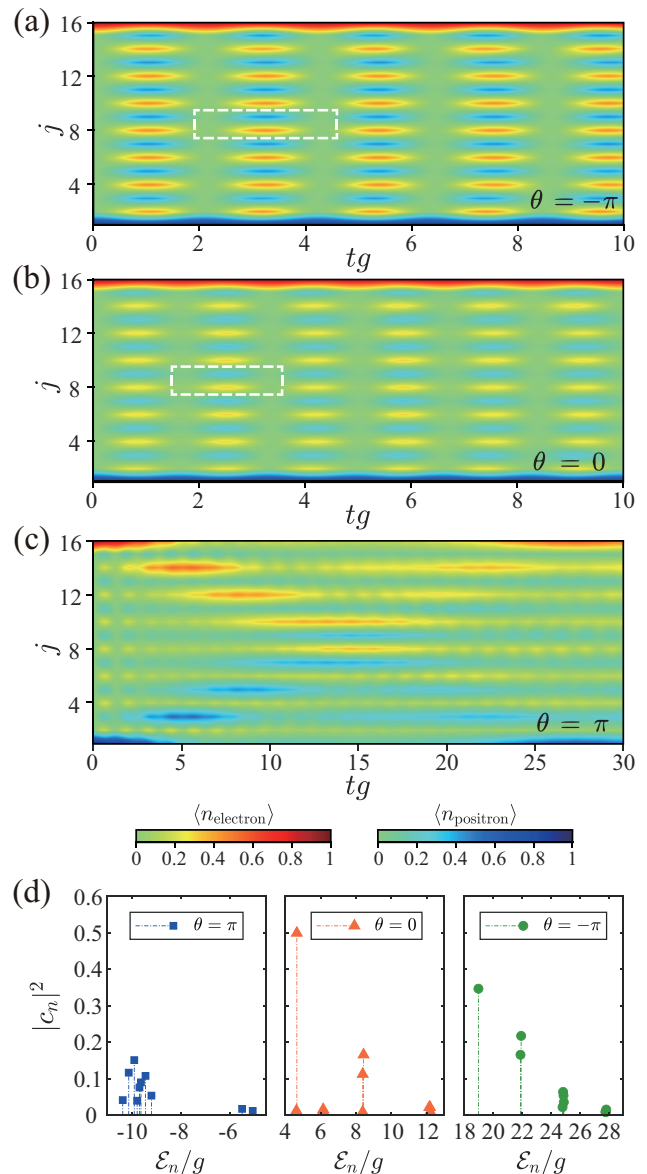


FIG. 4. (a)-(c) Dynamics of fermion occupations $\langle n_j \rangle$ for $\theta = -\pi$ [panel (a)], $\theta = 0$ [panel (b)], and $\theta = \pi$ [panel (c)], where the occupation status of the electron and positron are labeled by the red and blue color bars, respectively, the white boxes indicate the Schwinger mechanism. (d) Top 10 projection probabilities $|c_n|^2$ of the initial state $|\psi_0\rangle$ onto the eigenstates $|n\rangle$ of H under different θ value. In the calculation, we take $N = 16$, $m = 2g$, and $J = g = 1$.

To quantitatively explain the periodicity of $\langle n_j \rangle$ in Fig. 4, we calculate the projection probabilities of the initial state, denoted as $|c_n|^2 = |\langle n|\psi_0\rangle|^2$, where $|n\rangle$ is the eigenstate of H with energy \mathcal{E}_n . In Fig. 4(d), the largest ten values of $|c_n|^2$ are plotted against \mathcal{E}_n , with different θ values indicated using different markers. For comparison, we have aligned the ground state energy \mathcal{E}_0 of different θ values by shifting the spectra. From the data, it is evident that for $\theta = 0$ and $\theta = -\pi$, the initial state $|\psi_0\rangle$ is primarily composed of three high-energy eigenstates. These eigenstates exhibit a definite energy gap

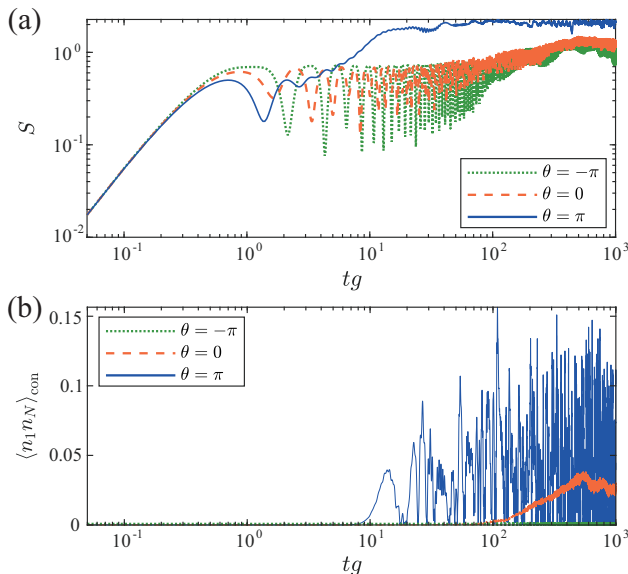


FIG. 5. (a) Dynamics of the bipartite entanglement entropy S for various cases of θ . For the confining cases, S exhibits a periodic oscillations and grows slowly due to Schwinger oscillation. On contrary, for the deconfining case, S presents a rapid increase. (b) Dynamics of the density-density correlator $\langle n_1 n_N \rangle_{\text{con}}$ between the two boundary fermions, for the confining cases, only weak correlation persisted. Oppositely, for deconfining case, correlation can grow rapidly. The parameters take $N = 16$, $m = 2J$, and $J = g = 1$.

$\Delta\mathcal{E}$, which determines the oscillating period of $\langle n_j \rangle$ in the way of $T = 2\pi/\Delta\mathcal{E}$. Specifically, for $\theta = 0$, $\Delta\mathcal{E} \approx 3.78g$ and $T \approx 1.66g^{-1}$, whereas for $\theta = -\pi$, $\Delta\mathcal{E} \approx 2.95g$ and $T \approx 2.13g^{-1}$. On the other hand, for the case of $\theta = \pi$, $|\psi_0\rangle$ consists of a broader spectrum of low-energy eigenstates. These states lack a consistent energy gap, which dictates the aperiodic behavior of $\langle n_j \rangle$.

The confining/deconfining characteristics can also be distinguished from the dynamics of the bipartite entanglement entropy

$$S = -\text{Tr} \rho_R \ln \rho_R, \quad (12)$$

where ρ_R is the reduced density matrix obtained by tracing out the degrees of freedom in one half of the chain. The evolution of S is displayed in Fig. 5(a), where the dotted, dashed, and solid lines correspond to $\theta = \{-\pi, 0, \pi\}$ respectively. The data reveals that, for the confining cases with $\theta = \{-\pi, 0\}$, S exhibits periodic oscillations and grows slowly in the time domain $t > 1$; until $t_c \sim 100g^{-1}$, S tends to approach saturation. In contrast, for the deconfining case with $\theta = \pi$, S undergoes a rapid increase in the interval $t \in [1, 10]$, following an approximate power-law scaling. It reaches equilibration at $t_c \sim 10g^{-1}$, which is an order of magnitude smaller compared to the former two cases. The time t_c coincides with the moment when the edge charges propagate to the center of the chain [see Fig. 4(c)].

We additionally calculate the dynamics of the connected

density correlation, defined by

$$\langle n_1 n_N \rangle_{\text{con}} = |\langle \psi_1^\dagger \psi_1 \psi_N^\dagger \psi_N \rangle - \langle \psi_1^\dagger \psi_1 \rangle \langle \psi_N^\dagger \psi_N \rangle|, \quad (13)$$

with the results being presented in Fig. 5(b). $\langle n_1 n_N \rangle_{\text{con}}$ quantifies the density-density correlation between the matter charges on the edges of the chain. Again, various line styles correspond to different cases of θ . It is anticipated that $\langle n_1 n_N \rangle_{\text{con}} = 0$ at $t = 0$, since the initial state is a product state. The weak correlation can persist for a considerable duration until t_c , beyond which significant correlations between the edge particles begin to develop. For the confining cases with $\theta = \{0, -\pi\}$, t_c is larger than $10^2 g^{-1}$. However, for the deconfining case $\theta = -\pi$, $t_c \sim 10g^{-1}$, being one order of magnitude smaller than in the previous cases. Therefore, the evolution of edge correlations provides a valuable metric for discerning different confinement statuses.

V. EXPERIMENTAL CONSIDERATION

We finally discuss the potential experimental realization using ultracold atoms. The spin-1 QLM has been theoretically proposed to be engineered from a generalized Bose-Hubbard model (BHM) [42], which can be implemented with ultracold bosonic gases confined in a superlattice, as illustrated in Fig. 6(a). Specifically, the atomic gas is governed by the Hamiltonian

$$\begin{aligned} H_{\text{BHM}} = & -\tilde{J} \sum_{l=1}^{L-1} (b_l^\dagger b_{l+1} + \text{h.c.}) + \frac{U}{2} \sum_{l=1}^L n_l (n_l - 1) \\ & + \sum_{l=1}^L \left[(-1)^l \frac{\delta}{2} + l\gamma + \frac{\chi_l}{2} \right] n_l + V \sum_{l=1}^{L-1} n_l n_{l+1} \\ & + W \sum_{l=1}^{\frac{L}{2}-1} n_{2l-1} n_{2l+1}, \end{aligned} \quad (14)$$

where $L = 2N$ is the total number of lattice sites, b_l and b_l^\dagger are local bosonic operators satisfying $[b_k, b_l^\dagger] = \delta_{k,l}$, and $n_l = b_l^\dagger b_l$. \tilde{J} is the hopping between neighboring sites, δ creates energy offsets between matter sites and gauge spins, and γ serves as a tilted potential. δ and γ help to eliminate gauge-breaking hoppings. χ_l is a four-site periodic term employed to realize the topological angle [27], i.e.,

$$\chi_l = \begin{cases} 0 & \text{if } l \bmod 2 = 0 \\ \chi & \text{if } l \bmod 4 = 1, \\ -\chi & \text{if } l \bmod 4 = 3 \end{cases}, \quad (15)$$

where $\chi = g\theta/\pi$. In the second line of Eq. (14), U is the on-site interaction, V and W are respectively the nearest-neighbor and next-nearest-neighbor interactions.

The generalized Bose-Hubbard model [Eq. (14)] serves as the foundation for realizing the spin-1 QLM [Eq. (1)] of length N . In this setup, the even lattice sites with $l \in \text{even}$ can only be singly occupied or empty, representing matter particles; whereas the occupancies at odd sites are restricted to

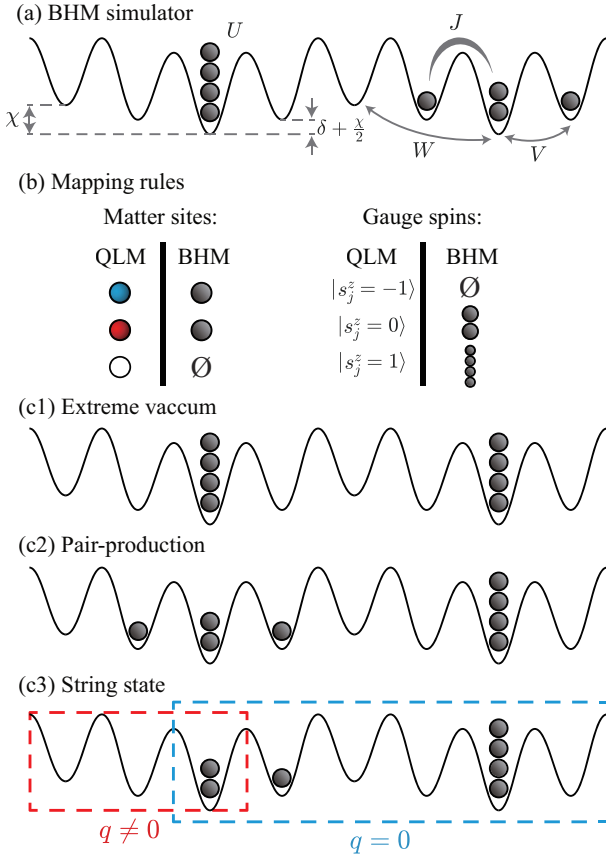


FIG. 6. (a) The schematics of BHM simulator on 1D superlattice, where the tilted potential γ is not shown. (b) The mapping relations between the particle representation of the BHM occupation and the particle-antiparticle picture of the QLM. (c) The preparation of the string state, with only the left boundary shown. (c1) The extreme vacuum state. (c2) Local particle-antiparticle pairs are generated using single-site addressing techniques. (c3) The string state is obtained by removing the outer particles. Blue and red boxes respectively indicate the physical and non-physical gauge sectors, with the latter providing a hard-wall boundary for the former.

$n_{l \in \text{odd}} = \{0, 2, 4\}$ to realize the three gauge spin states. The detailed mapping relations between the two models are presented in Fig. 6(b). To realize the gauge invariance in the $\mathbf{q} = \mathbf{0}$ sector, we focus on the following three configurations:

$$\begin{aligned}
 |C_1\rangle &= |0400\rangle_{\text{BHM}} \leftrightarrow |0_1 0_{-1}\rangle_{\text{QLM}}, \\
 |C_2\rangle &= |1210\rangle_{\text{BHM}} \leftrightarrow |1_0 1_{-1}\rangle_{\text{QLM}}, \\
 |C_3\rangle &= |0202\rangle_{\text{BHM}} \leftrightarrow |0_0 0_0\rangle_{\text{QLM}},
 \end{aligned} \quad (16)$$

where the notation $|n_l, n_{l+1}, n_{l+2}, n_{l+3}\rangle_{\text{BHM}}$ denotes the particle number representation of the BHM occupation status of four consecutive sites for $l \in \text{even}$, and the $|n_j, s_{j+1}, n_{j+2}, s_{j+3}\rangle_{\text{QLM}}$ represents the corresponding matter and gauge configuration in the QLM, where $j = l/2$. When $\tilde{J} = 0$, the bare energy of the three configurations

$|C_{1,2,3}\rangle$ are

$$\begin{aligned}
 \mathcal{E}_1 &= 6U - 2\delta \pm 2\chi, \\
 \mathcal{E}_2 &= U + 4V \pm \chi, \\
 \mathcal{E}_3 &= 2U + 8W - 2\delta,
 \end{aligned} \quad (17)$$

where the \pm determined by the bosonic lattice site index l according to Eq. (15). Based on this, all head-to-tail combinations of the three configurations span the entire Hilbert space in the physical sector.

Notably, there exist configurations that do not preserve gauge invariance. To circumvent these states, it is necessary to ensure that the bare energies of gauge-invariant configurations are nearly resonant, while those of the gauge-violating configurations are far-detuned from resonance. In the case of $U, V, W, \gamma \gg \tilde{J}$, it requires that

$$\begin{aligned}
 V &\approx \frac{5U}{4} - \frac{\delta}{2}, \\
 W &\approx -\frac{U}{2} + \delta + 2V \approx 2U.
 \end{aligned} \quad (18)$$

By applying the Schrieffer-Wolff transformation, we can derive the effective Hamiltonian of the Bose-Hubbard model within the gauge-invariant subspace, which takes the form of Eq. (1). The detailed coefficient relations are given by

$$g = 2U - 4W, \quad (19a)$$

$$m = -\frac{3}{2}U + \delta + 2V - 2W, \quad (19b)$$

$$J = \frac{8\sqrt{12}\tilde{J}^2(2\delta - 3U)}{(2\delta - 3U)^2 - 16\gamma^2}, \quad (19c)$$

where we have omitted the term $\propto \tilde{J}^2$ in Eq. (19a) and Eq. (19b) due to the perturbative nature of J . Additionally, χ is considered negligible in the expression of Eq. (19c) as $|\delta \pm \gamma| \gg |\chi|$ is satisfied [27].

The extreme vacuum state $|\psi_{\text{ev}}\rangle$ forms the basis for preparing string states, which is defined by

$$|\psi_{\text{ev}}\rangle = |\cdots 0400 \cdots\rangle_{\text{BHM}} \leftrightarrow |\cdots 0_1 0_{-1} \cdots\rangle_{\text{QLM}}. \quad (20)$$

This state, as shown in Fig. 6(c1), can be prepared systematically following a well-defined protocol [11, 27, 43]. The protocol begins with the system in a uniform superfluid (SF) state. The lattice potential is then gradually modified to establish the desired staggered structure by ramping the parameters γ and χ . Following this, the ratio U/\tilde{J} is tuned to induce a phase transition from the SF to a Mott insulator state, where deep lattice sites achieve a four-particle occupancy, shallow sites remain vacant, and even sites have an average occupancy satisfying $0 < \langle n_{l \in \text{even}} \rangle < 4$. Thereafter, spin-selective techniques [43] are applied to selectively remove particles from the even sites, resulting in the formation of the extreme vacuum state.

The string state $|\psi_{\text{str}}\rangle$ [Eq. (11)] is distinguished from $|\psi_{\text{ev}}\rangle$ by modifications only at the boundaries. Employing single-site addressing techniques [11, 27, 44] enables the generation of particle-antiparticle pairs at the boundaries of the vac-

uum state, as depicted in Fig. 6(c2). Subsequently, by locally removing the outer particles through a laser-induced resonant excitation, the string state can ultimately be obtained, as shown in Fig. 6(c3). At the left end of the chain, the left outer gauge sector (enclosed by the red box), with configuration $|012\dots\rangle_{\text{BHM}} \leftrightarrow |_{-1}0_0\dots\rangle_{\text{QLM}}$, does not belong to the physical sector $q = 0$. This ensures the rest of the chain (marked by the blue frame) operates consistently within the physical sector and experiences a hard-wall boundary. A similar strategy is also employed at the right end of the chain to achieve the complete particle distribution and boundary condition required for the string state.

VI. CONCLUSION

To conclude, we have presented a comprehensive investigation of partial confinement on the platform of the spin-1 quantum link model, a promising platform realizable with cold atoms in optical superlattices. The partial confinement is characterized by a dependency of confinement properties on the spatial arrangement of charged particles, manifested by the asymmetry of the equilibrium energy and the string

tension of the string state with respect to the charge ordering. In the non-equilibrium dynamics, string states with different charge orderings exhibit strikingly distinct dynamical features for such observables as local fermion occupations, bipartite entanglement entropy, and edge charge correlations. We have also elucidated that manipulating the topological angle can be an effective proxy for controlling charge ordering, thereby simplifying experimental procedures by obviating the need for direct charge manipulation. Given that the quantum link model is amenable to current experimental capabilities, our study offers a strategic avenue for exploring novel physics in gauge theories using state-of-the-art quantum simulators.

ACKNOWLEDGMENTS

L. C. acknowledges supports from the NSF of China (Grants No. 12174236) and from the fund for the Shanxi 1331 Project. W. Z. acknowledges supports from the NSF of China (Grants No. GG2030007011 and No. GG2030040453) and Innovation Program for Quantum Science and Technology (No. 2021ZD0302004).

-
- [1] K. G. Wilson, Confinement of quarks, *Phys. Rev. D* **10**, 2445 (1974).
- [2] C. G. Allan, R. Dashen, and D. J. Gross, A mechanism for quark confinement, *Physics Letters B* **66**, 375 (1977).
- [3] J. Greensite, *An introduction to the confinement problem*, Vol. 821 (Springer, 2011).
- [4] J. Schwinger, Gauge invariance and mass, *Phys. Rev.* **125**, 397 (1962).
- [5] S. Coleman, More about the massive schwinger model, *Annals of Physics* **101**, 239 (1976).
- [6] B. Svetitsky, Symmetry aspects of finite-temperature confinement transitions, *Physics Reports* **132**, 1 (1986).
- [7] T. Banks, L. Susskind, and J. Kogut, Strong-coupling calculations of lattice gauge theories: (1 + 1)-dimensional exercises, *Physical Review D* **13**, 1043 (1976).
- [8] J. B. Kogut, An introduction to lattice gauge theory and spin systems, *Rev. Mod. Phys.* **51**, 659 (1979).
- [9] S. Sachdev, Colloquium: Order and quantum phase transitions in the cuprate superconductors, *Rev. Mod. Phys.* **75**, 913 (2003).
- [10] Z. Alpichshev, F. Mahmood, G. Cao, and N. Gedik, Confinement-deconfinement transition as an indication of spin-liquid-type behavior in Na_2IrO_3 , *Phys. Rev. Lett.* **114**, 017203 (2015).
- [11] B. Yang, H. Sun, R. Ott, H.-Y. Wang, T. V. Zache, J. C. Halimeh, Z.-S. Yuan, P. Hauke, and J.-W. Pan, Observation of gauge invariance in a 71-site bose-hubbard quantum simulator, *Nature* **587**, 392 (2020).
- [12] A. Mil, T. V. Zache, A. Hegde, A. Xia, R. P. Bhatt, M. K. Oberthaler, P. Hauke, J. Berges, and F. Jendrzejewski, A scalable realization of local U(1) gauge invariance in cold atomic mixtures, *Science* **367**, 1128 (2020).
- [13] Z.-Y. Zhou, G.-X. Su, J. C. Halimeh, R. Ott, H. Sun, P. Hauke, B. Yang, Z.-S. Yuan, J. Berges, and J.-W. Pan, Thermalization dynamics of a gauge theory on a quantum simulator, *Science* **377**, 311 (2022), <https://www.science.org/doi/pdf/10.1126/science.abl6277>.
- [14] H.-Y. Wang, W.-Y. Zhang, Z. Yao, Y. Liu, Z.-H. Zhu, Y.-G. Zheng, X.-K. Wang, H. Zhai, Z.-S. Yuan, and J.-W. Pan, Interrelated Thermalization and Quantum Criticality in a Lattice Gauge Simulator, *Physical Review Letters* **131**, 050401 (2023).
- [15] W.-Y. Zhang, Y. Liu, Y. Cheng, M.-G. He, H.-Y. Wang, T.-Y. Wang, Z.-H. Zhu, G.-X. Su, Z.-Y. Zhou, Y.-G. Zheng, H. Sun, B. Yang, P. Hauke, W. Zheng, J. C. Halimeh, Z.-S. Yuan, and J.-W. Pan, Observation of microscopic confinement dynamics by a tunable topological θ -angle (2023), [arXiv:2306.11794 \[cond-mat.quant-gas\]](https://arxiv.org/abs/2306.11794).
- [16] C. Kokail, C. Maier, R. Van Bijnen, T. Brydges, M. K. Joshi, P. Jurcevic, C. A. Muschik, P. Silvi, R. Blatt, C. F. Roos, and P. Zoller, Self-verifying variational quantum simulation of lattice models, *Nature* **569**, 355 (2019).
- [17] E. A. Martinez, C. A. Muschik, P. Schindler, D. Nigg, A. Erhard, M. Heyl, P. Hauke, M. Dalmonte, T. Monz, P. Zoller, and R. Blatt, Real-time dynamics of lattice gauge theories with a few-qubit quantum computer, *Nature* **534**, 516 (2016).
- [18] S. Chandrasekharan and U.-J. Wiese, Quantum link models: A discrete approach to gauge theories, *Nuclear Physics B* **492**, 455 (1997).
- [19] U. Wiese, Ultracold quantum gases and lattice systems: quantum simulation of lattice gauge theories, *Annalen der Physik* **525**, 777 (2013).
- [20] M. C. Bañuls, R. Blatt, J. Catani, A. Celi, J. I. Cirac, M. Dalmonte, L. Fallani, K. Jansen, M. Lewenstein, S. Montangero, C. A. Muschik, B. Reznik, E. Rico, L. Tagliacozzo, K. Van Acoleyen, F. Verstraete, U.-J. Wiese, M. Wingate, J. Zakrzewski, and P. Zoller, Simulating lattice gauge theories within quantum technologies, *The European Physical Journal D* **74**, 165 (2020).

- [21] E. Zohar, J. I. Cirac, and B. Reznik, Quantum simulations of lattice gauge theories using ultracold atoms in optical lattices, *Reports on Progress in Physics* **79**, 014401 (2016).
- [22] L. Chen, F. Zhu, Z. Tang, and C. Gao, Ultracold quantum simulation of high-energy physics: lattice gauge theory and its realization in cold atoms, *Emerging Science and Technology* **2**, 49 (2023).
- [23] M. Troyer and U.-J. Wiese, Computational complexity and fundamental limitations to fermionic quantum monte carlo simulations, *Phys. Rev. Lett.* **94**, 170201 (2005).
- [24] D. Banerjee, M. Dalmonte, M. Müller, E. Rico, P. Stebler, U.-J. Wiese, and P. Zoller, Atomic quantum simulation of dynamical gauge fields coupled to fermionic matter: From string breaking to evolution after a quench, *Phys. Rev. Lett.* **109**, 175302 (2012).
- [25] F. M. Surace, P. P. Mazza, G. Giudici, A. Lerose, A. Gambassi, and M. Dalmonte, Lattice gauge theories and string dynamics in rydberg atom quantum simulators, *Phys. Rev. X* **10**, 021041 (2020).
- [26] Y. Cheng, S. Liu, W. Zheng, P. Zhang, and H. Zhai, Tunable confinement-deconfinement transition in an ultracold-atom quantum simulator, *PRX Quantum* **3**, 040317 (2022).
- [27] J. C. Halimeh, I. P. McCulloch, B. Yang, and P. Hauke, Tuning the topological θ -angle in cold-atom quantum simulators of gauge theories, *PRX Quantum* **3**, 040316 (2022).
- [28] E. Zohar, J. I. Cirac, and B. Reznik, Simulating Compact Quantum Electrodynamics with Ultracold Atoms: Probing Confinement and Nonperturbative Effects, *Physical Review Letters* **109**, 125302 (2012).
- [29] Y. Cheng and C. Li, Gauge theory description of rydberg atom arrays with a tunable blockade radius, *Phys. Rev. B* **107**, 094302 (2023).
- [30] B. Buyens, J. Haegeman, H. Verschelde, F. Verstraete, and K. Van Acoleyen, Confinement and string breaking for qcd_2 in the hamiltonian picture, *Phys. Rev. X* **6**, 041040 (2016).
- [31] H.-Y. Qi and W. Zheng, Gauge violation spectroscopy of synthetic gauge theories, *Physical Review Research* **6**, 013047 (2024).
- [32] J. Mildenerger, W. Mruzekiewicz, J. C. Halimeh, Z. Jiang, and P. Hauke, Probing confinement in a \mathbb{Z}_2 lattice gauge theory on a quantum computer (2022), [arXiv:2203.08905 \[quant-ph\]](https://arxiv.org/abs/2203.08905).
- [33] S. Kühn, J. I. Cirac, and M.-C. Bañuls, Quantum simulation of the schwinger model: A study of feasibility, *Phys. Rev. A* **90**, 042305 (2014).
- [34] R. Jackiw and C. Rebbi, Vacuum periodicity in a yang-mills quantum theory, *Phys. Rev. Lett.* **37**, 172 (1976).
- [35] N. Batakis and G. Lazarides, Structure of the gauge theory vacuum at finite temperatures, *Phys. Rev. D* **18**, 4710 (1978).
- [36] G. 't Hooft, Computation of the quantum effects due to a four-dimensional pseudoparticle, *Phys. Rev. D* **14**, 3432 (1976).
- [37] Y.-P. Huang, D. Banerjee, and M. Heyl, Dynamical quantum phase transitions in $u(1)$ quantum link models, *Phys. Rev. Lett.* **122**, 250401 (2019).
- [38] P. Hauke, D. Marcos, M. Dalmonte, and P. Zoller, Quantum simulation of a lattice schwinger model in a chain of trapped ions, *Phys. Rev. X* **3**, 041018 (2013).
- [39] D. Marcos, P. Rabl, E. Rico, and P. Zoller, Superconducting Circuits for Quantum Simulation of Dynamical Gauge Fields, *Physical Review Letters* **111**, 110504 (2013).
- [40] C. Gao, J. Liu, M. Chang, H. Pu, and L. Chen, Synthetic $u(1)$ gauge invariance in a spin-1 bose gas, *Phys. Rev. Res.* **4**, L042018 (2022).
- [41] C. Gao, Z. Tang, F. Zhu, Y. Zhang, H. Pu, and L. Chen, Non-thermal dynamics in a spin- $\frac{1}{2}$ lattice schwinger model, *Phys. Rev. B* **107**, 104302 (2023).
- [42] J. Osborne, B. Yang, I. P. McCulloch, P. Hauke, and J. C. Halimeh, *Spin- $U(1)$ Quantum Link Models with Dynamical Matter on a Quantum Simulator* (2023), [arXiv:2305.06368 \[cond-mat, physics:hep-lat, physics:quant-ph\]](https://arxiv.org/abs/2305.06368).
- [43] W.-Y. Zhang, M.-G. He, H. Sun, Y.-G. Zheng, Y. Liu, A. Luo, H.-Y. Wang, Z.-H. Zhu, P.-Y. Qiu, Y.-C. Shen, X.-K. Wang, W. Lin, S.-T. Yu, B.-C. Li, B. Xiao, M.-D. Li, Y.-M. Yang, X. Jiang, H.-N. Dai, Y. Zhou, X. Ma, Z.-S. Yuan, and J.-W. Pan, Scalable multipartite entanglement created by spin exchange in an optical lattice, *Phys. Rev. Lett.* **131**, 073401 (2023).
- [44] B. Yang, H.-N. Dai, H. Sun, A. Reingruber, Z.-S. Yuan, and J.-W. Pan, Spin-dependent optical superlattice, *Phys. Rev. A* **96**, 011602 (2017).